



Harmonizing microstructures and enhancing mechanical resilience: Novel powder metallurgy approach for Zn–Mg alloys

Anna Boukalová^a, Jiří Kubásek^{a,*}, David Nečas^a, Peter Minárik^c, Črtomir Donik^b,
Drahomír Dvorský^{a,d}, Dalibor Vojtěch^a, Alena Michalcová^a, Matjaž Godec^b, Irena Paulin^b

^a Department of Metals and Corrosion Engineering, University of Chemistry and Technology, Technická 6, Prague, 6, 166 28, Czech Republic

^b Institute of Metals and Technology, Lepi Pot 11, SI-1000, Ljubljana, Slovenia

^c Charles University, Faculty of Mathematics and Physics, Department of Physics of Materials, Ke Karlovu 5, 121 16, Prague, Czech Republic

^d Department of Functional Materials, Institute of Physics of the Czech Academy of Sciences, Na Slovance 1999/2, 182 21, Prague, 8, Czech Republic

ARTICLE INFO

Handling editor: M Meyers

Keywords:

Zinc
Magnesium
Biodegradable
Powder metallurgy
Harmonic structure

ABSTRACT

Zinc alloys are recognised for their excellent biocompatibility and favourable corrosion rates, making them suitable for bioabsorbable implants. However, their mechanical properties necessitate improvement to fulfil the rigorous requirements of biomedical applications. This research focuses on engineering pseudo-harmonic structures within zinc alloys through a comprehensive method combining mechanical alloying, spark plasma sintering, and hot extrusion techniques. This fabrication process results in a composite material characterised by a soft core surrounded by a continuous, three-dimensional, ultrafine-grained hard shell. The experiment involved blending pure zinc with Zn–1Mg alloy powder, leading to the formation of both ductile zinc and fine-grained Zn–1Mg regions. While the Mg₂Zn₁₁ intermetallic phase was found to enhance the alloy's mechanical strength, the presence of oxide shells adversely affected the material's properties. The elimination of these shells via hot extrusion markedly improved the alloy's tensile strength, reaching an average value of tensile strength of 333 ± 7 MPa. This study provides significant insights into the material engineering of zinc-based alloys for biodegradable implant applications, demonstrating a viable approach to optimising their mechanical performance.

1. Introduction

Due to its favourable biocompatibility [1], zinc was proposed as a material for biodegradable implant manufacturing [2]. Zinc plays an important role in the human body, with approximately 80 % of its content distributed in bones, muscles, skin and skin appendages [3]. Notably, its corrosion rate and corrosion products well-tolerable for the human body are among the advantages of zinc over other candidates for biodegradable components like magnesium and iron [4].

However, adequate mechanical properties are necessary for orthopaedic applications – these include a recommended yield strength of a minimum of 230 MPa, a tensile strength of a minimum of 300 MPa and elongation to failure of at least 15 % [5]. Regrettably, pure zinc does not meet these requirements and, therefore, alloying in combination with various processing techniques of materials is often examined. Magnesium is in this case one of the most common alloying elements of zinc [4, 6]. Since the solubility of magnesium in a solid solution of zinc is very

low, the intermetallic phases, namely Mg₂Zn₁₁ and MgZn₂, begin to precipitate at very low magnesium contents [7]. The presence of these phases has a strong effect on the resulting mechanical properties especially enhancing zinc's strength up to 1 wt % of Mg content. However, at higher concentrations of magnesium, an excessive amount of coarse and brittle intermetallic Mg₂Zn₁₁ phases form in the material's structure leading to low strength, plasticity and toughness [2].

Materials in the Zn–Mg system, when produced through casting, exhibit substandard mechanical characteristics as identified in multiple studies [2,8,9]. To combat these deficiencies, researchers have turned to hot extrusion techniques, which notably enhance mechanical attributes, yet still do not meet the requirements [10–12]. Consequently, the quest for processing methodologies capable of achieving desired properties while simultaneously advancing both strength and ductility remains a paramount objective. Recent investigations within the last half-decade have delved into approaches like hydrostatic extrusion, Equal Channel Angular Pressing (ECAP), and powder metallurgy for crafting these

* Corresponding author.

E-mail address: kubasekj@vscht.cz (J. Kubásek).

<https://doi.org/10.1016/j.jmrt.2024.06.223>

Received 13 May 2024; Received in revised form 26 June 2024; Accepted 28 June 2024

Available online 4 July 2024

2238-7854/© 2024 The Authors. Published by Elsevier B.V. This is an open access article under the CC BY license (<http://creativecommons.org/licenses/by/4.0/>).

alloys, resulting in a refined microstructure [13–18]. Among these methods, hydrostatic extrusion emerges as particularly promising, supporting extrusion at reduced temperatures to inhibit zinc recrystallisation. Notably, this methodology has yielded materials displaying outstanding mechanical properties, surpassing 400 MPa in ultimate tensile strength and 25% in elongation to failure [13,14].

In the presented paper we wish to go even beyond these studies and adopt the idea of heterostructured materials, particularly materials with harmonic structure, enabling the simultaneous improvement of both strength and elongation. Heterostructured materials are composed of heterogeneous regions, and domains, with different mechanical or physical properties. The combination of the domains' properties allows to achieve a synergistic effect in the resulting heterostructured material [19–21]. Harmonic materials are a type of heterostructured materials consisting of coarse-grained cores enclosed in a continuous 3D network of an ultrafine-grained skeleton [22–24], as shown in Fig. 1. These materials are generally produced by powder metallurgy in two different ways. The first method involves gentle mechanical milling, which produces powder particles with a finer grain size on the surface (shell) and a larger grain size inside the particle (core). In the second case, milling of two initial powders, one coarse-grained with large particles and the other fine-grained with smaller particles is performed. During this process, the fine-grained particles are repeatedly coated on the coarse-grained powder particles [22]. The latter possibility was adapted in the presented work. The coarse-grained powder was selected to be pure zinc, whereas mechanically alloyed powder of Zn–1Mg (wt. %) was used as the fine-grained powder fraction. Zn–1Mg was chosen over pure zinc which is characterized by a very low recrystallisation temperature ($-12\text{ }^{\circ}\text{C}$), rendering it challenging to achieve a fine-grained structure at room temperatures [25]. The production of Zn–1Mg by mechanical alloying is another key factor considered in this work, because this technology enables the preparation of materials in non-equilibrium conditions recognized by the formation of metastable phases and ultrafine grains [26,27]. Further application of fast consolidation processes like spark plasma sintering (SPS) technique enables preservation of such microstructure even for the compacted material [28]. The weakness of consolidation by SPS is related to the formation of oxide shells on the surface of the original powder particles inside the microstructure [18,29,30] reducing the mechanical properties of prepared materials. Therefore, the extrusion process is also considered to break the microstructure of SPS products.

In summary, this work illustrates a novel approach to zinc-based materials production by adopting a harmonic structure model, potentially resulting in enhanced mechanical properties of the materials produced.

2. Materials and methods

2.1. Mechanical alloying

Firstly, the Zn–1Mg alloy was prepared by mechanical alloying in the Retsch E-max mill. For the preparation of this alloy, two ZrO_2 milling vessels with ZrO_2 milling balls of 1 cm in diameter were used. Into both of these vessels, 30 g of the mixture obtained by mixing the zinc and

magnesium powders in a given proportion were placed together with 0.04 g of stearic acid to prevent the particles from clumping and sticking to the milling balls and walls of the vessels. The mass ratio of used milling balls to the powder in the vessel was equivalent to 5:1. Before the mechanical alloying, the milling vessels were rinsed with argon atmosphere to decrease the oxygen content causing undesirable oxidation of the powders. The powders were mechanically alloyed for 4 h with 800 rotations per minute (RPM) and within the temperature range of 28–40 $^{\circ}\text{C}$. The direction of the rotation changed every 10 min.

2.2. Spark plasma sintering (SPS) and extrusion (Ex)

The powders used for the compaction by spark plasma sintering (SPS) technique were of two different particle sizes. The pure zinc powder constituted of particle size in the range of 63–100 μm , whereas the size of the particles of the Zn–1Mg alloy powder was smaller than 45 μm . The compaction was performed in FCT Systeme HP-D 10 under an argon atmosphere at 300 $^{\circ}\text{C}$ for 10 min and using the compaction force of 25 kN. Some of the prepared materials were consequently extruded at 200 $^{\circ}\text{C}$ at the speed of 0.2 mm/s with an extrusion ratio (ER) equal to 10 to minimize the effect of oxide shells presented in the materials after SPS. The designation of the prepared materials used in this work is summarised in Table 1.

2.3. Microstructure characterisation

The prepared materials were wet ground using SiC papers of various grit sizes (P240–P4000) and subsequently polished using the combination of D2 diamond polishing paste (URdiamant) and Eposil Non-Dry suspension (QATM). For EBSD analyses the samples were further ion-polished by Leica EM RES102 (5 kV, impact angle of 5 $^{\circ}$). The microstructure of the polished materials was studied by optical microscopy (OM – Nikon Eclipse MA200 using NIS Elements software) and scanning electron microscopy (SEM – Tescan Lyra 3) equipped with an EDX Analyser (Oxford Instruments Aztec). EBSD analysis was performed using an FEI 3D Quanta 3D field-emission-gun DualBeam scanning electron microscope equipped with an EBSD detector TSL/EDAX Hikari. The data were processed using the OIM Analysis 7.3 software. The raw data set was partially cleaned by one step of confidence index (CI) standardisation and one iteration of grain dilatation, and only points with $\text{CI} > 0.1$ were used for the analysis. During the EBSD measurement, the binning was set to 4x4, the accelerating voltage was 20 kV and the current 32 nA. The step size was chosen to be 50 nm.

The ImageJ software was used to evaluate the grain size and size of the intermetallic phases. In this software, the area of a particular grain was measured based on which the equivalent diameter of the grain was calculated according to the equation $d_{eq} = \sqrt{4S/\pi}$.

Similarly, the ImageJ software was also used for the evaluation of the distribution of the harmonic structure's domains. Using the threshold function, the area of zinc and Zn–1Mg domains was evaluated based on the different brightness of the two domains presented in the material.

The samples studied by transmission electron microscopy (TEM-

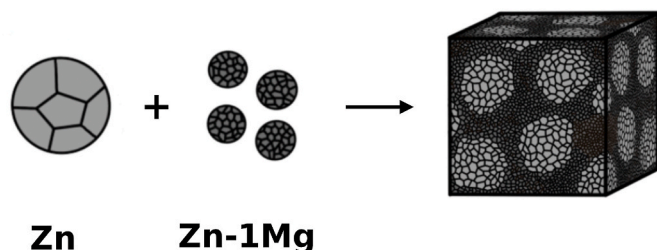


Fig. 1. The formation of harmonic structure.

Table 1

Designation of prepared materials.

Material's designation	Zn (wt. %)	Zn–1Mg (wt. %)	Processing
Zn_{SPS}	100	–	SPS: 300 $^{\circ}\text{C}$, 10 min, 25 kN
$\text{Zn–1Mg}_{\text{SPS}}$	–	100	
$\text{Zn} + \text{Zn–1Mg}_{30:70\text{SPS}}$	30	70	
$\text{Zn} + \text{Zn–1Mg}_{50:50\text{SPS}}$	50	50	
$\text{Zn} + \text{Zn–1Mg}_{70:30\text{SPS}}$	70	30	
$\text{Zn}_{\text{SPS}} + \text{Ex}$	100	–	SPS: 300 $^{\circ}\text{C}$, 10 min, 25 kN
$\text{Zn–1Mg}_{\text{SPS}} + \text{Ex}$	–	100	
$\text{Zn} + \text{Zn–1Mg}_{50:50\text{SPS}} + \text{Ex}$	50	50	+ extrusion: 200 $^{\circ}\text{C}$, ER 10

EFTEM Jeol 2200 FS, 300 kV, LaB₆) were firstly ground by SiC papers of various grit sizes (P240–P4000) to the width <100 μm. The final width of the samples, about 40 μm, was attained by Ar ions polishing in the Gatan Precision Ion Polishing System (Gatan, Pleasanton, CA, USA).

The phase composition of initial powders and prepared compact materials were further studied by X-ray diffraction (PANalytical X'Pert³ with a Cu anode – $\lambda = 1.5406 \text{ \AA}$) using HighScore Plus and Topas 3 software.

2.4. Mechanical properties

Firstly, powders were embedded in the resin (CEM1000 Blue). The prepared samples were then ground with SiC grinding papers (P800–P4000). The Vickers microhardness was subsequently measured on the Future-Tech microhardness tester FM-700 at a load of 10 g for 10 s. The average value was calculated from 20 measurements, along with the standard deviation. The hardness profile was measured on a compact material polished by a procedure described in Chapter 2.3 at a load of 10 g with a distance between each indentation equal to three times the length of the diagonal of the largest indentation measured.

The compressive and bending tests were performed on the Lab-Test5.250SP1 testing machine at 25 °C and a constant speed of 1 mm/min. The cuboid samples for the compressive tests were of size 3.5 × 3.5 × 5 mm. The bending test was performed on samples with width and height both equal to 3.5 mm with a bending span of 12 mm.

The tensile tests were performed using the Instron 8872 machine on samples of specified dimensions shown in Fig. 2. These tests were performed at 25 °C at a strain rate of 1.5 mm/min.

3. Results

3.1. Phase composition

The phase compositions of the powders of pure Zn and Zn–1Mg alloy and the materials with elements of harmonic structure are shown in Fig. 3. The XRD analysis showed the content of the Mg₂Zn₁₁ phase to be 6 wt % in Zn–1Mg powder. Based on the calculations derived from these results, about half of the total magnesium content in the Zn–1Mg alloy is presented in the solid solution of zinc. Therefore, it can be seen that the processing of zinc and magnesium powders by mechanical alloying has a positive effect on the increased solubility of magnesium in the solid solution of zinc, which is, in equilibrium conditions, close to zero. After the compaction by SPS, the content of the Mg₂Zn₁₁ intermetallic phase slightly decreased (~4 wt %) and no new intermetallic phases occurred in Zn–1Mg^{SPS} after sintering. The content of the Mg₂Zn₁₁ phase corresponds to 1–2 wt % in all the harmonic structured materials and traces of ZnO have been detected.

3.2. Microstructure

3.2.1. Products by SPS

The microstructure of compacted Zn–1Mg alloy (Fig. 4a) was composed of zinc grains ($d_{eq} = 626 \pm 240 \text{ nm}$) and darker areas ($d_{eq} = 396 \pm 125 \text{ nm}$). The EDX analysis (see the supplementary data) determined the content of magnesium in these areas to be 5.2 wt %, which corresponds to the Mg₂Zn₁₁ phase (6.3 wt % of Mg). Minor difference is related to the effect of the surrounding area of small particles occupied

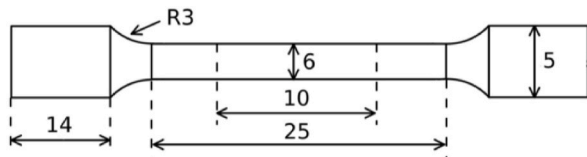


Fig. 2. The tensile test sample (values are given in millimetres).

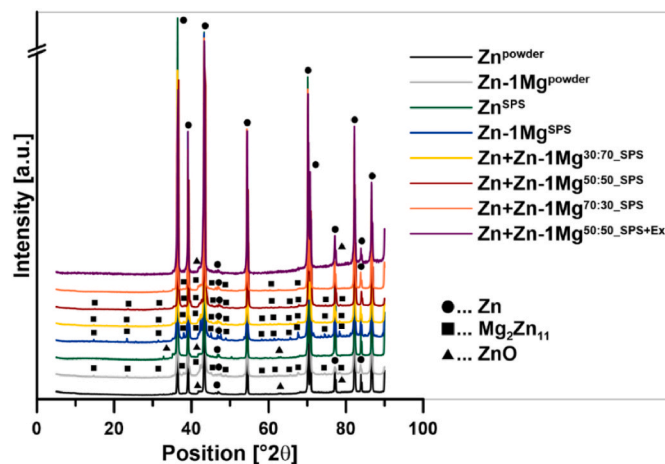


Fig. 3. The phase composition of initial powders and compact materials.

by zinc solid solution. Furthermore, the presence of the Mg₂Zn₁₁ phase was confirmed by X-ray diffraction analysis. Besides, the EDX analysis in SEM microscope showed the content of magnesium dissolved in a solid solution of zinc is equal to 0.4 wt%. EDX analysis in the TEM microscope additionally confirmed the occurrence of very fine Mg₂Zn₁₁ phases (see the supplementary data) and the zinc and magnesium oxides at the grain boundaries. The fine particles of oxides appear in Fig. 4b as light areas. The local EDX analysis of these oxides showed an increased content of magnesium (~3 wt %).

Microstructures of the materials with elements of harmonic structure are shown in Fig. 5 (additional figures and EDX results can be found in the supplementary data) and are composed of two domains: coarse-grained pure zinc domain and fine-grained Zn–1Mg domain. Pure zinc domains appear as light areas with the grain size $d_{eq} = 12 \pm 7 \mu\text{m}$. Zn–1Mg domains appear slightly darker. The Zn–1Mg domain consists of zinc solid solution grains ($d_{eq} = 815 \pm 342 \text{ nm}$), intermetallic phases Mg₂Zn₁₁ ($d_{eq} = 380 \pm 134 \text{ nm}$), and fine oxide particles of zinc and magnesium. At the interface of these two domains, an oxide shell was observed (Fig. 6). In Fig. 5a–c, microstructures of materials with various ratios among Zn and Zn–1Mg components in the form of input powders are visible. Based on the results obtained by image analysis, it can be said that prepared materials exhibited a relatively homogenous distribution of the two domains in the bulk.

More detailed analyses of the microstructure including grain orientation and texture were performed using EBSD measurement (Fig. 7). Furthermore, the grain size distribution for the Zn–1Mg component in materials with harmonic structure is presented in Fig. 7b. The majority of grains is below 1 μm although some grains reached the size up to 2 μm. To better visualise texture differences in both (soft and hard) domains, separated analyses were done (Fig. 7 c and d). The soft areas are occupied by coarse-grained zinc with weak (10 $\bar{1}0$) fibre texture, although this can be related to the large size of zinc grains with specific orientation and relatively small map region, while hard areas are occupied by extremely fine-grained Zn–1Mg characterised by random orientation.

3.2.2. Product by extrusion

The microstructure of the extruded material Zn + Zn–1Mg^{50:50_SPS + Ex} (Fig. 8) shows the occurrence of texture in the extrusion direction. The average grain size of the Zn domain reached $13 \pm 8 \mu\text{m}$, which is similar to the material produced by SPS. These domains remain surrounded by Zn–1Mg, and therefore the harmonic nature of the material is preserved even after the extrusion. Additionally, oxide shells are partially broken. Following the breakage of the oxide shells, very fine oxide particles are present primarily on the interface of the two Zn and Zn–1Mg and distributed throughout the Zn–1Mg domain (Fig. 9). The grain size of the

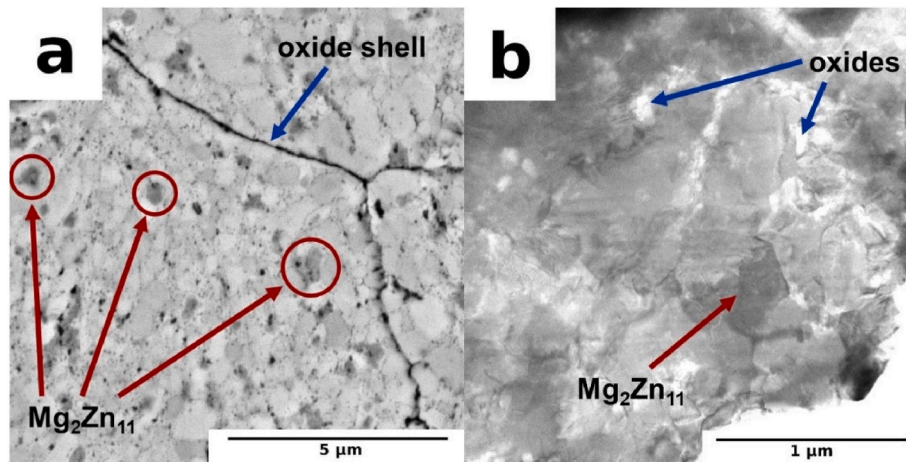


Fig. 4. The microstructure of Zn–1Mg^{SPS}: (a) SEM, (b) detail by TEM.

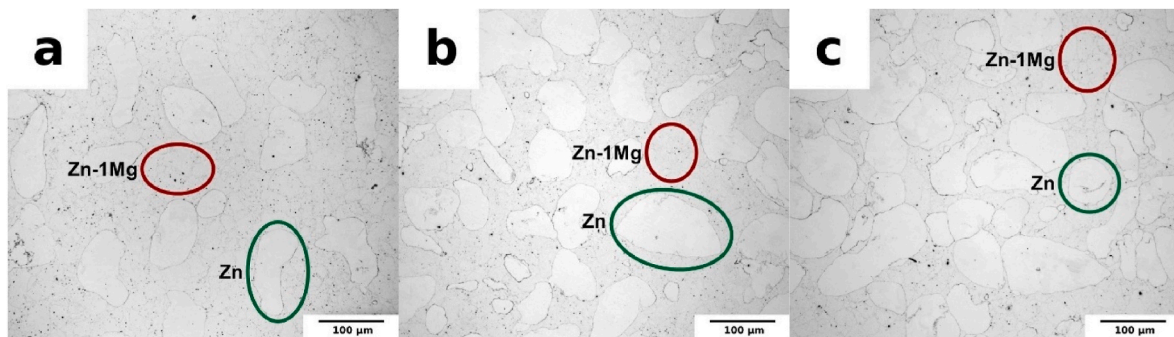


Fig. 5. The microstructure of the Zn + Zn–1Mg materials with various weight ratios of Zn: Zn–1Mg domains: (a) 30:70, (b) 50:50, (c) 70:30.

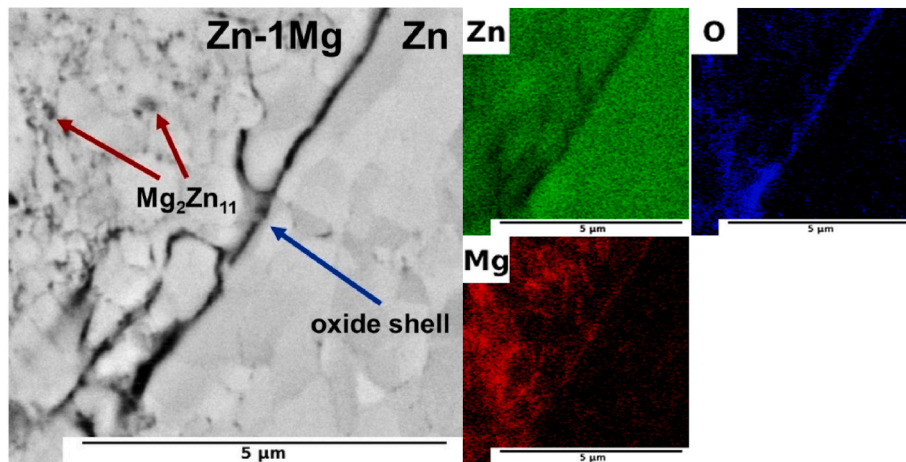


Fig. 6. The distribution of elements in the Zn + Zn–1Mg^{50:50,SPS} material (SEM-EDX).

zinc solid solution in the Zn–1Mg domain after extrusion was equal to $d_{eq} = 842 \pm 309$ nm. Although the XRD analysis did not show the presence of the Mg_2Zn_{11} phase, dark areas ($d_{eq} = 401 \pm 116$ nm) with an enhanced concentration of magnesium can be seen in the microstructure of Zn + Zn–1Mg^{50:50,SPS + Ex}. Also, a trend following the enhanced concentrations of magnesium and oxygen can be observed in Fig. 10.

EBSD analyses further confirmed that the nature of coarse-grained and ultrafine-grained areas is preserved after extrusion (Fig. 11). For a larger EBSD map documenting the distribution of zinc soft zones and grain size inside these areas, the reader is referred to the supplementary data (Fig. S5). The distribution of grain size in Zn–1Mg domains

(Fig. 11b) is similar for extruded samples as was observed for SPS. Also, the texture of both soft and hard domains is preserved after extrusion. Although the recrystallisation of zinc during the hot extrusion takes place, due to the high temperature (200 °C), the zinc grains become coarse. At the same time, it is predicted that the nucleation of new grains takes place at the interface with Zn–1Mg domains, causing rather the random orientation in soft domains. Zn–1Mg domains contain small intermetallic phases and oxides which work as nucleation sites for recrystallisation and also block the grain boundaries against their movement and related grain growth.

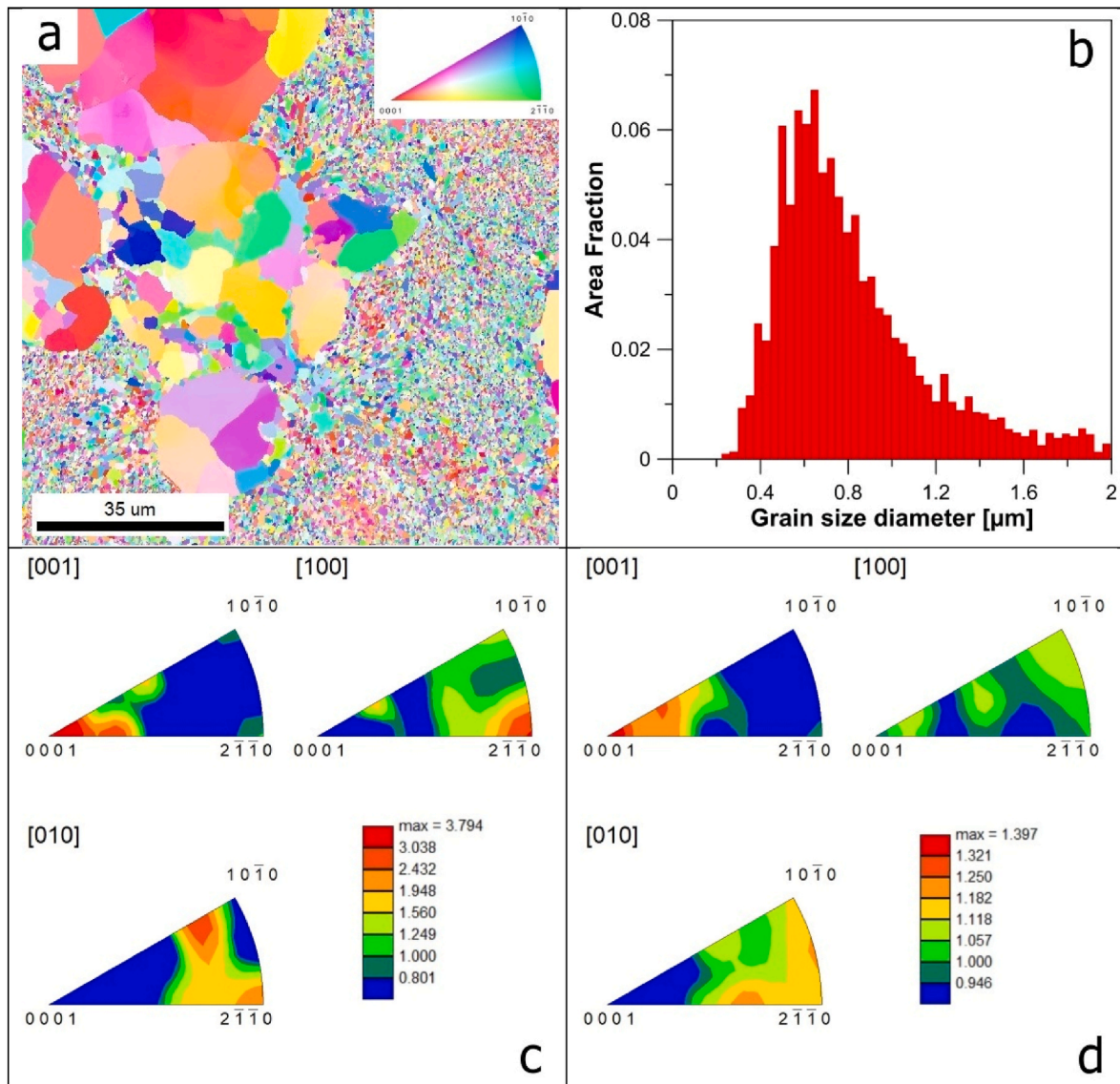


Fig. 7. EBSD analyses of the Zn + Zn-1Mg^{50:50_SPS}. a) IPF map, b) grain size distribution for Zn-1Mg domains, c) IPF for Zn, d) IPF for Zn-1Mg.

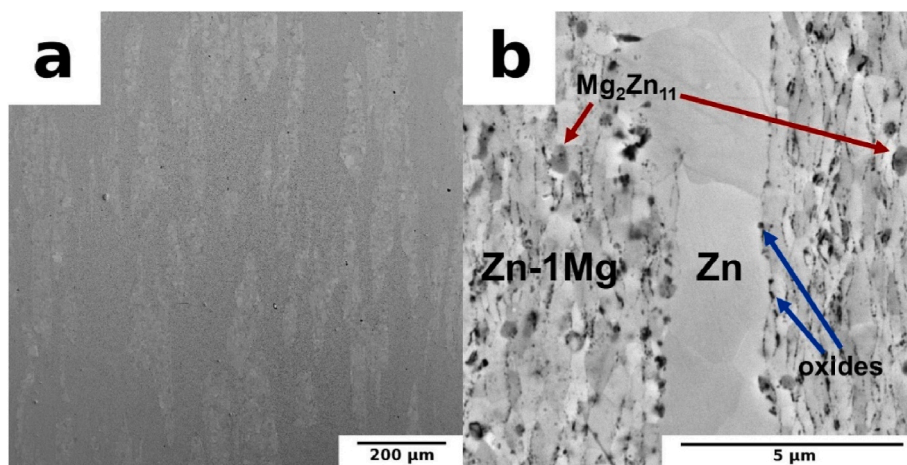


Fig. 8. The microstructure of the hot extruded material Zn + Zn-1Mg^{50:50_SPS} + Ex.

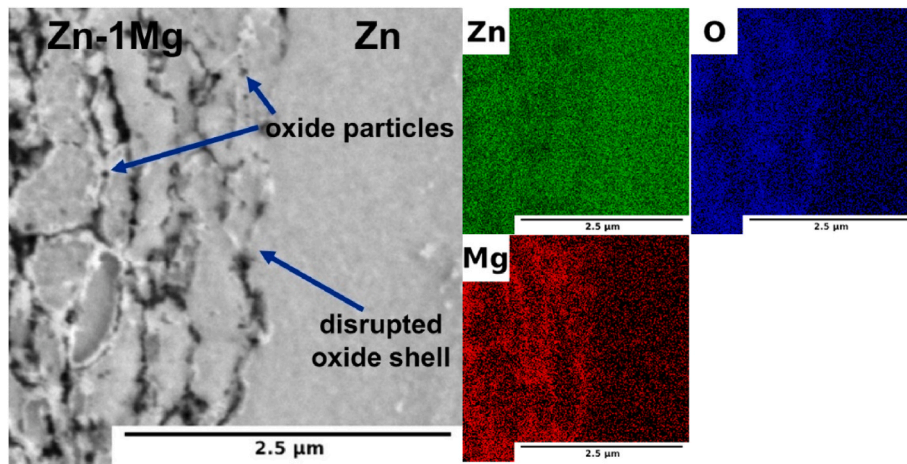


Fig. 9. The map of the element distribution in the Zn + Zn-1Mg^{50:50_SPS + Ex} material (SEM-EDX).

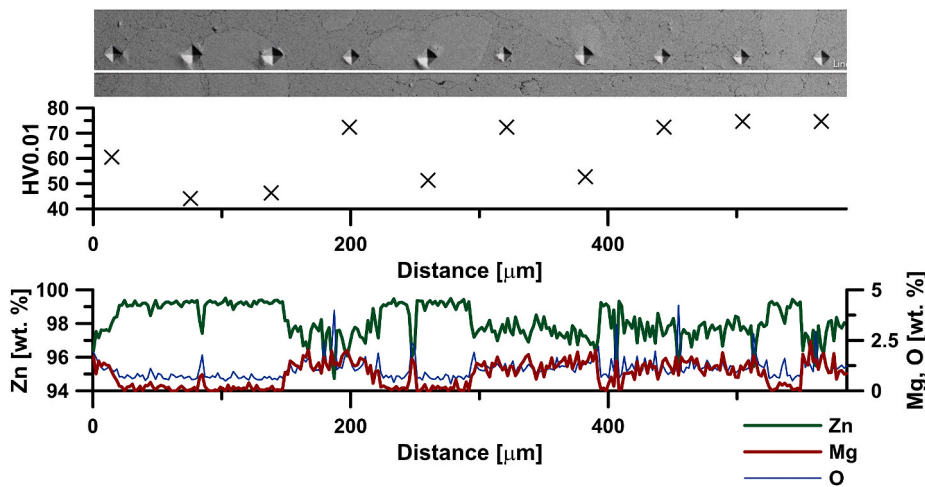


Fig. 10. The hardness profile with the changes in chemical composition for the Zn + Zn-1Mg^{50:50_SPS} material.

3.3. Mechanical properties

Vickers hardness was measured for powders of pure zinc and Zn-1Mg at a load of 10 g. The alloying of zinc by magnesium resulted in enhanced hardness. Whereas pure zinc exhibited a hardness of 36.9 ± 1.9 HV0.01, the hardness of Zn-1Mg was measured to be 86.1 ± 4.3 HV0.01.

A hardness profile was measured for material Zn + Zn-1Mg^{50:50_SPS} and is shown in Fig. 10 along with the changes in chemical composition, which was measured along the white line. In this profile, an influence of changes in chemical and phase composition within the material on the measured microhardness values can be observed. As mentioned earlier, materials with harmonic structures are composed of soft domains encapsulated in hard fine-grained domains. It can be seen that the hardness of the material is higher with the increasing content of magnesium. Therefore, while the microhardness is low and approaches approximately 54.4 HV0.01 in the soft domains of pure zinc, with higher magnesium content the microhardness increases and reaches up to 102 HV0.01 in the Zn-1Mg alloy domain. Also, the oxygen content can be observed to increase at the boundaries of the original powder particles.

Compressive tests were measured both for materials compacted by the SPS technique and materials that were further processed by extrusion. The results obtained from these tests can be seen in Fig. 12. Relatively low compressive yield strength and a wide plastic deformation region can be observed for Zn^{SPS}. Zn-1Mg^{SPS} has more than three

times higher compressive yield strength than Zn^{SPS}. The influence of magnesium alloying on the enhancement of zinc strength properties can be attributed to the presence of Mg₂Zn₁₁ [2]. While no fracture occurred for the Zn^{SPS} during the compression test, Zn-1Mg^{SPS} material achieved a low value of relative strain to fracture. For materials with harmonic structure, it can be observed that after the combination of plastic zinc and hard Zn-1Mg, the ultimate compressive strength of resulting materials decreased compared to the Zn-1Mg^{SPS}. Also, the effect of variation in the content of soft and hard domains can be observed – while the higher fraction of Zn-1Mg supports higher strength, it worsens the material's plasticity. The effect of oxide shell disruption by extrusion on the increase of mechanical properties is evident for all three materials (Zn^{SPS + Ex}, Zn-1Mg^{SPS + Ex}, Zn + Zn-1Mg^{50:50_SPS + Ex}). However, the Zn + Zn-1Mg^{50:50_SPS + Ex} material showed a synergistic effect of harmonic microstructure on both strength and plasticity resulting in the highest mechanical properties among the prepared materials.

Results obtained from the bending strength test are shown in Fig. 12b. From all the tested materials, only pure zinc exhibited plastic behaviour as other materials exhibited brittle behaviour under bending. The Zn-1Mg^{SPS} alloy showed the highest flexural strength of these materials, with a value of 93 ± 2 MPa. When comparing materials with different ratios of pure zinc and Zn-1Mg domains, it can be observed that the different content of these regions in the microstructure of the materials did not have a significant effect on the resulting mechanical properties in the bend.

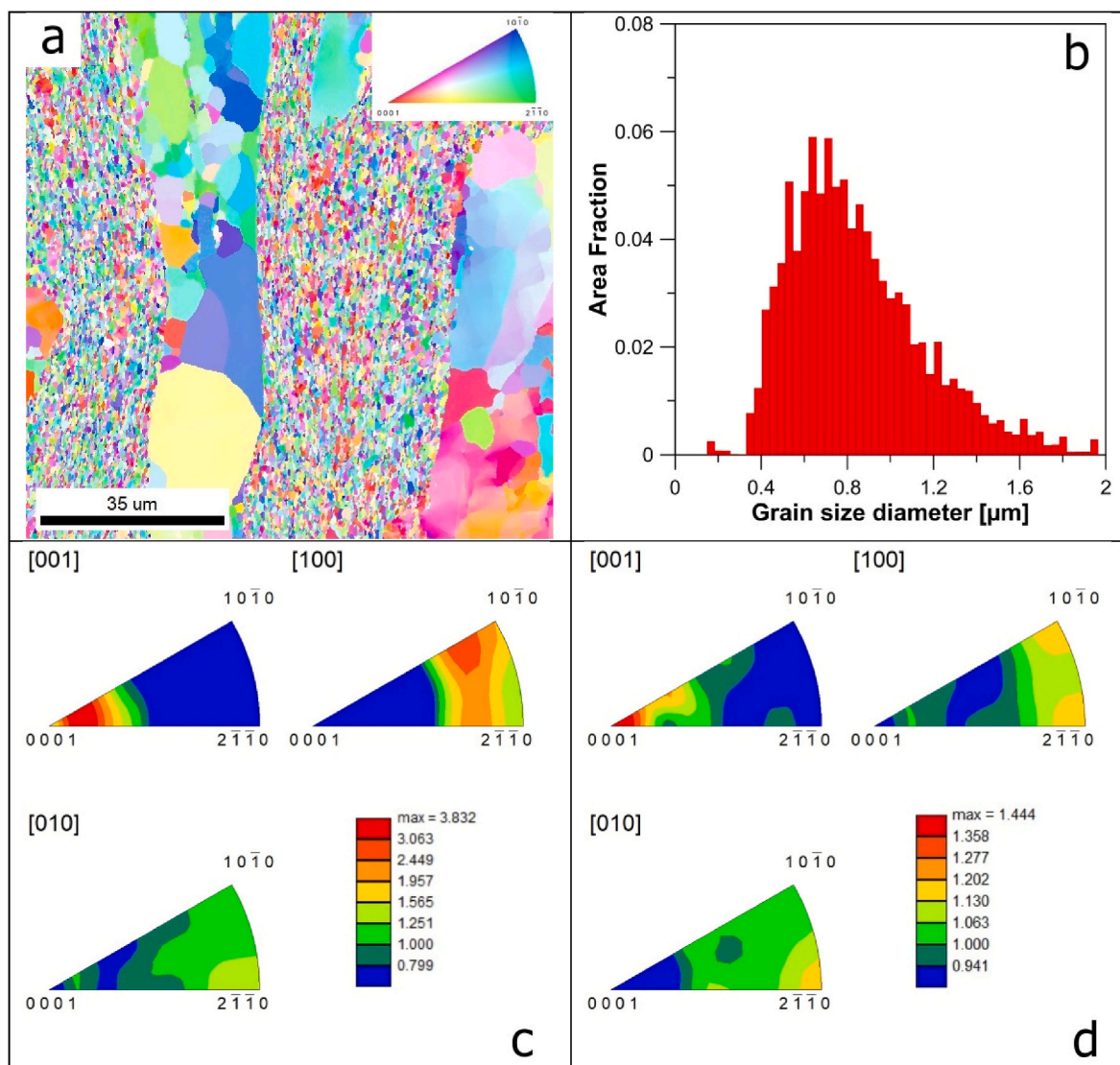


Fig. 11. EBSD analyses of the Zn + Zn-1Mg^{50:50}SPS + Ex. a) IPF map, b) grain size distribution for Zn-1Mg domains, c) IPF for Zn, d) IPF for Zn-1Mg.

The tensile tests were measured only for extruded materials. Extruded zinc exhibited the most plastic behaviour, although its tensile strength is rather poor. A significant increase in mechanical performance was observed for the Zn-1Mg alloy, which reached the ultimate tensile strength of more than 400 MPa. However, the elongation to fracture was poor, 5 ± 2 %. On the contrary, a material combining Zn and Zn-1Mg domains reached a rather high tensile strength of 333 ± 7 MPa and acceptable ductility of 13 ± 2 %.

4. Discussion

4.1. Microstructure

4.1.1. Products by SPS

The combination of mechanical alloying and spark plasma sintering compaction resulted in materials with extremely fine grains in Zn-1Mg domains. The resulting grain size of zinc solid solution is slightly higher compared to the size obtained by similar techniques in the work presented by Nečas et al. [30] and is significantly lower than those prepared by conventional techniques that usually correspond to tens or even hundreds of μm [2,9,26]. Together with the coarse grain size of soft zinc domains ($11.1 \pm 4.4 \mu\text{m}$), the appropriate conditions like in harmonic structures are reached. To effectively enhance mechanical properties,

the microstructure of harmonic structures should consist of soft cores enclosed in a hard fine-grained skeleton [21]. In the presented study it is shown that the ratio of hard domains in the material should be at least 50 % to ensure the envelopment of soft domains, although some coagulation of zinc domains was observed for both Zn + Zn-1Mg^{50:50}SPS and Zn + Zn-1Mg^{30:70}SPS. The larger area of the domains' interface for Zn + Zn-1Mg^{50:50}SPS is another advantage of this composition [31]. On the contrary, the area of the domains' interfaces is decreased in the Zn + Zn-1Mg^{30:70}SPS material. Furthermore, the increased content of pure zinc domains in Zn + Zn-1Mg^{70:30}SPS material caused the formation of hard islands of Zn-1Mg surrounded by the soft region of pure zinc. Therefore no significant synergistic effect and increase in mechanical properties is expected [31].

The results of the EDX analysis (Fig. 6) indicate partial diffusion of magnesium from the powder particle volume to its interface, which resulted in the enhanced content of magnesium of 3 wt %. Due to the high affinity of magnesium to oxygen, magnesium oxides may form at the interface of the original powder particles. In this case, the magnesium can utilise the oxygen trapped between the powder particles during compaction or a reaction with ZnO may occur. In this way, the powder particles may be partially depleted of magnesium when compared to the mechanically alloyed powder. However, due to the rather low content of oxides in the microstructure, they were not detected by XRD analysis.

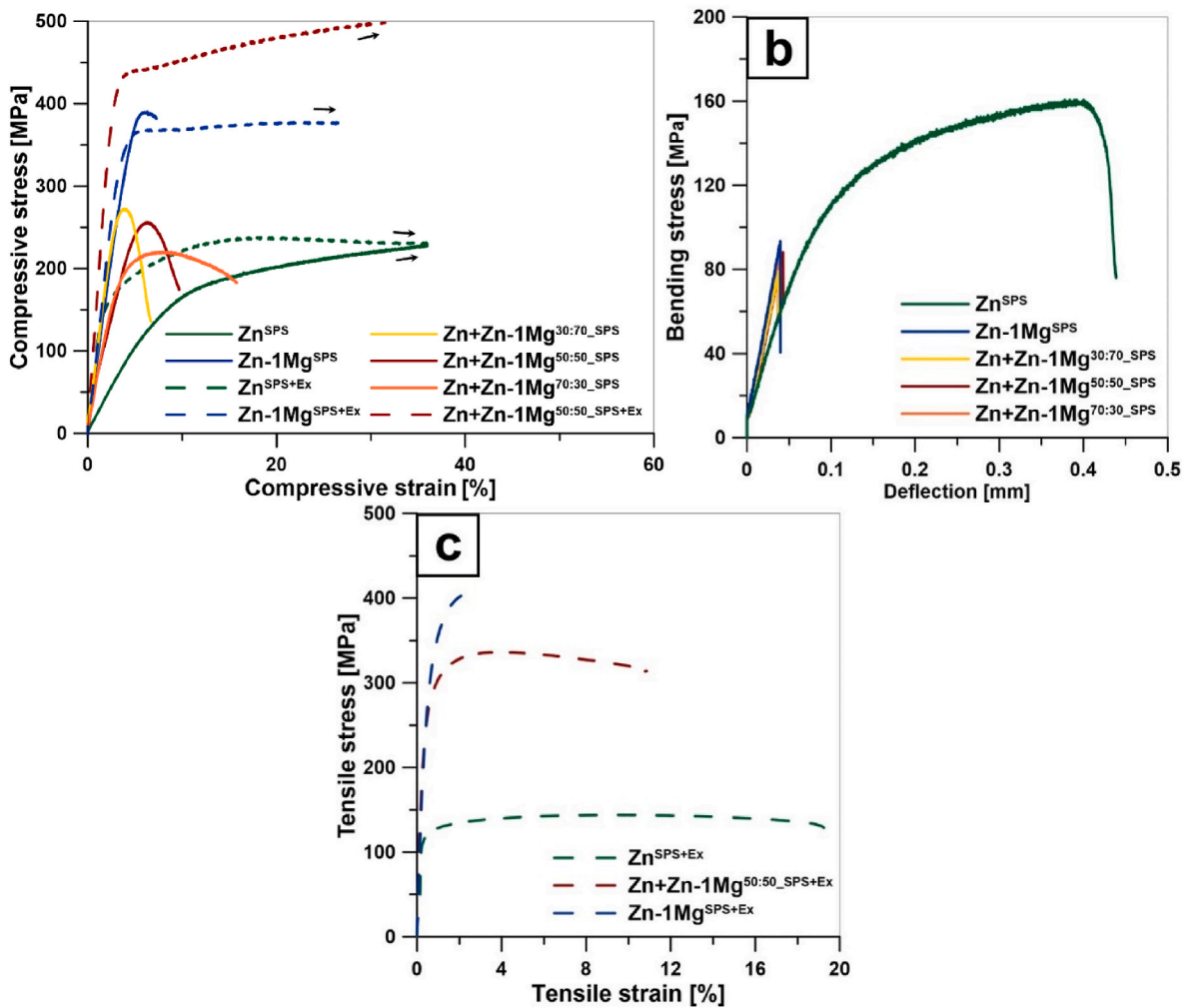


Fig. 12. (a) Compressive test: the true stress-strain diagram, (b) 3-point bending test: the engineering stress-deflection diagram, (c) Tensile test: Engineering stress-strain diagram.

4.1.2. Product by extrusion

The thermo-mechanical processing by extrusion resulted in the partial breakage of the oxide shells, and also in the formation of texture in the extrusion direction. This morphology provides significant enhancement of strength and plasticity [31,32]. The breaking of the oxide shells generated very fine oxide particles in the microstructure of extruded materials. These particles, though brittle, are expected to act as reinforcement by acting as barriers to dislocation movement, thereby contributing to the overall stability and performance of the material when compared to those non-extruded containing continuous oxide shells [33]. Besides these particles can block the grain boundaries to suppress microstructure coarsening. In general, enhanced concentrations of oxygen were observed together with magnesium. This phenomenon can be attributed to the higher affinity of magnesium to oxygen rather than to zinc.

4.2. Mechanical properties

The solubility of magnesium in zinc is nearly zero at ambient temperatures [7]. However, mechanical alloying enables the formation of a non-equilibrium state of the material with an oversaturated solid solution of alloying element in the matrix [27]. We can thus prepare a solid solution of magnesium in zinc that contains higher magnesium concentrations than those theoretically expected to be stable according to the phase diagram. Our first aim was to prepare the sample by mixing pure zinc powder with powder of Zn-1Mg alloy, in which magnesium

would be completely dissolved in a solid solution. However, the microhardness of the suggested state was equal to 40.3 HV1 with a standard deviation of 3.8 and thus comparable to that of pure zinc. Such observation is in good agreement with the work by Chen et al. [34], where the strengthening effect of magnesium dissolved in the solid solution of zinc on the material strength was estimated to be only 15.7 MPa for 1 wt % of magnesium [34]. Therefore, we rather selected to work with Zn-1Mg alloy mechanically alloyed at conditions leading to the homogeneously distributed fine Mg₂Zn₁₁ intermetallic phases and ultra-fine grains. Such material is characterized by increased hardness and strength and more appropriately defines the hard zones in harmonic microstructure [18,35].

To consider the strengthening effect in prepared composite materials let's firstly look at the properties of reference materials, namely Zn and Zn-1Mg consolidated by SPS and SPS + Ex. The mechanical behaviour of the materials in compression is shown in Fig. 12a. Zinc is occupied by coarse grains enabling a free path for dislocation motion supporting plasticity but the strengthening contribution from pure zinc is rather weak. Finally, the compressive yield strength (CYS) is rather low for SPSed and extruded samples. On the contrary, the Zn-1Mg is an ultrafine-grained material with a higher value of CYS. Such improvement is attributed to several strengthening mechanisms, with grain boundary strengthening being one of the most significant. This contribution is often described by the Hall-Petch relationship (1). In this equation, σ_y stands for the yield strength, σ_0 and K are constants specific for the given material and d is the grain size. Another possibility, how to

describe the relationship between yield strength and grain size is suggested based on the unified model considering grain boundary sliding (2). This model makes sense for zinc-based materials, especially with low grain size and also due to the low recrystallisation temperature of zinc. In equation (2), G represents the shear modulus, k is the Boltzmann's constant, b is the Burgers vector, δ is the grain boundary width, $\dot{\epsilon}$ is the deformation rate, D_{gb} represents grain boundary diffusion coefficient, T is thermodynamic temperature, and d_t is grain size estimated as the mean linear intercept length.

$$\sigma_y = \sigma_0 + K \cdot d^{-1/2} \quad (1)$$

$$\sigma \approx \sqrt{\frac{\sqrt{3}GkT}{2d_t b^2} \ln\left(\frac{\dot{\epsilon} d_t^3}{2\delta D_{gb}} + 1\right)} \quad (2)$$

Based on the equation (2) and observed grain size, the contribution to the yield strength for both Zn^{SPS} and Zn^{SPS+Ex} can be estimated as ≈ 80 MPa (average grain size = $8 \pm 4 \mu m$ and $9 \pm 4 \mu m$, respectively). Similarly for $Zn-1Mg^{SPS}$ and $Zn-1Mg^{SPS+Ex}$, the contribution to the yield strength can be estimated as ≈ 170 and 160 MPa, respectively [36].

The strengthening by solid solution supported by magnesium dissolved in zinc is generally considered as another strengthening mechanism. However, the effect of magnesium in solid solution is poor even at the solution concentration of 1 wt %, which is a significantly higher value than in our $Zn-1Mg$, the increase of the YS compared to the pure zinc is very limited (15.7 MPa) [34]. Therefore, we expect that the solid solution strengthening will be very similar for all materials independent of Mg content with the expected contribution to the YS approximately 38 MPa (the value for pure zinc). Considering grain boundary and solid solution strengthening, we can estimate CYS for Zn^{SPS+Ex} approximately about 117 MPa, close to the experimentally observed value of 133 MPa and for $Zn-1Mg^{SPS}$ and $Zn-1Mg^{SPS+Ex}$ as 208 and 198 MPa, which brings slightly lower values compared to the experimentally measured CYS of 285 and 266 MPa, respectively (Table 2).

Another strengthening mechanism for consideration includes strengthening by intermediate phases/precipitates or dislocation strengthening. Dislocation strengthening may be roughly estimated by equation (3), where ρ_{GND} corresponds to the geometrically necessary dislocation related to the deformation of the zinc matrix ($10^{12} m^{-2}$ obtained from GND maps using EBSD), μ and b are the shear modulus of Zn (35 GPa) and the Burgers vector for basal slip in Zn ($2.67 \cdot 10^{-10} m$). This leads to the value of 4 MPa. Some care is necessary regarding this estimation due to the low sensitivity of the selected technique (EBSD) to the performed analyses and simplification of approximation to the dislocations in the basal plane. We did not perform EBSD analyses for Zn^{SPS} and Zn^{SPS+Ex} , but we expect that the dislocation concentration should be on a similar level or even lower because both materials contain large equiaxed grains as a consequence of grain coarsening during compaction, and therefore majority of dislocation would be stored in grain boundaries.

$$\sigma_D = M \alpha \mu b \rho_{GND}^{1/2} \quad (3)$$

After the inclusion of dislocation strengthening contribution, the predicted values of CYS do not change significantly. The residual discrepancy between estimated values of CYS and experimentally measured values may be related to the presence of intermetallic phases Mg_2Zn_{11} and/or oxide particles participating by another strengthening contribution. The effect of Mg_2Zn_{11} can be calculated using equations (3–5) adopted from the literature [37]. In these relations, σ_p represents the contribution of intermetallic phases (Mg_2Zn_{11}) to the YS values, γ is the accommodation factor, μ^M is the shear modulus of zinc matrix (35 GPa), μ^P is the shear modulus of Mg_2Zn_{11} phase (33 GPa), V represents volume fraction of Mg_2Zn_{11} phase in the material ($\approx 6\%$), ϵ corresponds to the unrelaxed plastic strain (estimated as 0.007 according to the literature [38]) and ν is Poisson ratio of Mg_2Zn_{11} (0.29).

$$\sigma_p = 4\phi \gamma \mu^M V \epsilon \quad (3a)$$

$$\gamma = \frac{1}{2(1-\nu)} \quad (4)$$

$$\phi = \frac{\mu^P}{\mu^P - \gamma(\mu^P - \mu^M)} \quad (5)$$

Based on this calculation, the effect of Mg_2Zn_{11} on the TYS value corresponds to the 43 MPa. The missing contribution ($\approx 20-30$ MPa) for $Zn-Mg$ materials can be related to the strengthening by oxide particles or/and also to some approximations in suggested calculations. It's worth mentioning that considered intermetallic particles and oxides are mainly distributed at the grain boundaries. Therefore, they support the thermal stability of the structure and protect the material against grain coarsening.

The compressive stress-strain curves of $Zn + Zn-1Mg$ composites produced by SPS are between both SPSed Zn and SPSed $Zn-1Mg$ indicating dependence on the fraction of both main components. Whereas with a higher content of pure zinc the material shows an increase in plasticity, the higher content of $Zn-1Mg$ domains causes an increase in the yield strength. The CYS value of these materials can be roughly estimated by the rule of mixture considering Zn^{SPS} and $Zn-1Mg^{SPS}$. However, this calculation leads to a value which is close to the experimentally obtained CYS (Table 2). This may indicate a rather weak synergistic effect of both components in the produced composite material. Such results are probably caused by the presence of oxide shells on the surface of the initial powder particles, which prevented the exploitation of the potential synergistic behaviour by distracting the desirable dislocation behaviour on the interface of the soft and hard domains [24]. The adverse effect of the presence of oxide shells can also be predicted from the results of 3-point bending tests (Fig. 12b). The bending test is significantly more sensitive to structural defects and inhomogeneities in the material structure than the compression test. The low measured flexural strengths can therefore be attributed to the presence of brittle oxide shells enabling the easier and fast fracture propagation.

Table 2
Summary of mechanical properties' values for studied materials.

	Compressive test		Tensile test			3-point bending test
	$R_{d0,2}$ (MPa)	$^a R_{d0,2}$ (MPa)	$R_{p0,2}$ (MPa)	R_m (MPa)	E (%)	R_{m0} (MPa)
Zn^{SPS}	88 ± 16		–	–	–	162 ± 2
Zn^{SPS+Ex}	133 ± 3		109 ± 7	145 ± 1	19 ± 4	–
$Zn-1Mg^{SPS}$	285 ± 14		–	–	–	93 ± 2
$Zn-1Mg^{SPS+Ex}$	266 ± 35		265 ± 9	403 ± 7	5 ± 2	–
$Zn + Zn-1Mg^{30:70,SPS}$	227 ± 4	226	–	–	–	79 ± 1
$Zn + Zn-1Mg^{50:50,SPS}$	213 ± 21	187	–	–	–	82 ± 6
$Zn + Zn-1Mg^{70:30,SPS}$	176 ± 6	147	–	–	–	83 ± 1
$Zn + Zn-1Mg^{50:50,SPS+Ex}$	359 ± 8	200	251 ± 7	333 ± 7	13 ± 2	–

^a Calculated by the rule of mixture using Zn^{SPS+Ex} and Zn^{SPS+Ex} .

To break the oxides, an extrusion process has been performed for the Zn + Zn–1Mg composite characterised after SPS by the largest area of interface between Zn and Zn–1Mg. As discussed earlier, the nature of the material remained preserved with soft areas elongated in the direction of extrusion surrounded by hard domains. These conditions brought indeed interesting results regarding compressive behaviour while the stress-strain curve is located above both Zn^{SPS + Ex} and Zn–1Mg^{SPS + Ex} and the calculated CYS (200 MPa, calculated by the rule of mixture) is significantly lower compared to the experimentally obtained 359 MPa (Table 2). This indicates some further strengthening contributions and we believe that this is mainly related to the hetero-deformation induced (HDI) strengthening.

To further analyse the properties of Zn + Zn–1Mg^{SPS + Ex}, a tensile test was performed for composite material and also for Zn^{SPS + Ex} and Zn–1Mg^{SPS + Ex} (Fig. 12c) with the latter one characterised by high tensile yield strength (TYS ≈ 265 MPa) but low elongation to fracture (E ≈ 5%). The work hardening is the key factor affecting ductility. It is known that this process is limited in nano-grained materials because dislocations are attracted to grain boundaries instead of mutual interaction [19]. As a consequence, the material is losing ductility. In our case, the majority of grains is in the range of ultrafine-grained (grain size below 1 μm), which brings a limited free path for dislocation movement, and therefore faster hardening. On the contrary, compressive testing does not need work hardening to maintain stability, and therefore the sample can sustain large compressive strains (Fig. 12a). To better visualise the work hardening of studied materials, the true stress–true strain tensile diagrams are presented in Fig. 14. Only the region of uniform plastic deformation is considered and the blue curve is calculated for composite material based on the contribution of Zn^{SPS + Ex} and Zn–1Mg^{SPS + Ex} by the rule of mixture. Measured values of true stress for composite material (red curve) are located above the calculated blue curve. Furthermore, both the elongation to fracture (Fig. 13c) and uniform elongation (Fig. 13) are increased compared to the Zn–1Mg^{SPS + Ex}. All curves were fitted according to the Hollomon law (6), where σ represents true stress, ϵ true strain, n strain hardening exponent, and K strength coefficient. The R^2 values were in the range between 0.94 and 0.99.

$$\sigma = K\epsilon^n \quad (6)$$

The average values of evaluated constants are presented in Table 3. The strain hardening coefficient of zinc-based alloys is generally observed in the range of 0.1–0.3, which is also similar to this work. The

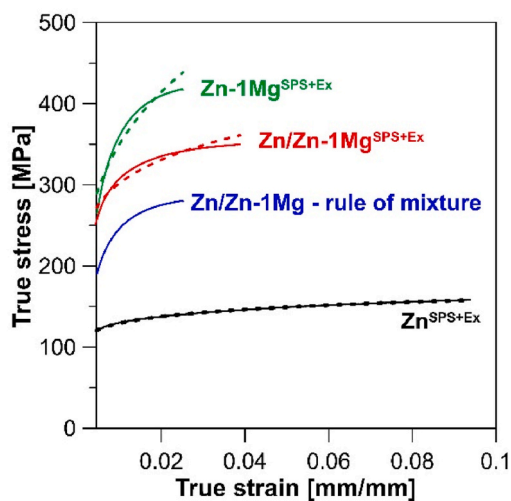


Fig. 13. True stress – true strain tensile curves considering only the area of uniform elongation for materials prepared by a combination of SPS and extrusion. The dashed lines represent the calculated curve based on the Hollomon law and the blue curve is calculated according to the rule of mixture.

highest value of n corresponds to the higher rate of strain hardening for Zn–1Mg^{Ex + SPS}. On the contrary, Zn^{Ex + SPS} is characterised by the lowest value of n as a consequence of larger grain size and fewer grain boundaries, which act as barriers to dislocation motion. As a result, the dislocation density increases more gradually during deformation, leading to lower strain hardening. The strength coefficient K for zinc alloys varies widely depending on the alloy composition, processing conditions, and microstructure. For common commercial zinc alloys such as Zamak, the strength coefficient K typically ranges from about 200 MPa to 400 MPa, for pure zinc, the K value is generally lower, often around 100–200 MPa, reflecting its relatively lower strength. In the case of high-strength zinc alloys, the K values range from 400 MPa to 600 MPa and can be even higher. The obtained results agree well with these general observations and assign the Zn + Zn–1Mg^{Ex + SPS} to the group of high-strength zinc alloys with medium strain hardening rate.

In Fig. 14, we further demonstrate the fracture surfaces after the tensile test. The fracture surface of Zn^{SPS + Ex} (Fig. 14 a,b) exhibits a mix of smooth regions suggesting that the material undergoes uniform deformation and small voids or dimples of varying sizes, which are indicative of ductile fracture. These dimples are formed by the nucleation, growth, and coalescence of voids during plastic deformation. The density and size distribution of these dimples suggest that the material is capable of undergoing extensive plastic deformation before failure, supporting its higher ductility. The fracture surface of the Zn–1Mg^{SPS + Ex} (Fig. 14 c,d) shows features indicative of a combination of ductile–brittle fracture. The surface appears rough with numerous cleavage facets, which are characteristic for low-energy fracture processes. The presence of these facets suggests that the material failed along specific crystallographic planes, typical for brittle materials. The presence of micro-cracks and small dimples can be also observed, which indicates limited plastic deformation before fracture. The fracture surface of the Zn + Zn–1Mg^{SPS + Ex} (Fig. 14 e,f) combines the characteristics of previous materials. The areas occupied by coarse-grained zinc are characterised by a mix of flat regions and zones with dimple morphology indicating plasticity in these domains. The Zn–1Mg domains are occupied mainly by numerous cleavage facets but in a minor amount the signs of plastic deformation are observed. In summary, the presented results well document that zinc fraction is the bearer of the material plasticity, while Zn–1Mg fraction is responsible for the increase in material strength.

4.2.1. Mechanical performance in comparison with the state-of-the-art

Fig. 15 compares the mechanical properties of Zn–Mg materials prepared by various techniques and the material prepared in this work. The mechanical properties required for materials intended for orthopaedic biodegradable devices are also indicated. Mechanical properties of the materials prepared by casting are generally insufficient for these utilisations as they possess both low strength and plasticity. Thermo-mechanical processing by extrusion leads to an enhancement of these properties. The mechanical characteristics of specific materials after extrusion depends on several factors, such as extrusion temperature, extrusion ratio and extrusion speed. The characteristics of these materials differ widely in different studies, implying that the materials sharing the same chemical composition but undergoing different processing conditions may exhibit substantial variations in their mechanical properties. Regrettably, the number of materials reaching the desired properties is still fairly low, even after the extrusion. Shen et al. [39] prepared a Zn–1.2 Mg (wt. %) material by hot extrusion at 250 °C with extrusion ratio 36, that achieved sufficient mechanical properties – ultimate tensile strength of 363 MPa and elongation to failure of 21.3 % [39]. The extrusion ratio used in this work was significantly higher than the rest studies suggesting significant microstructure refinement. Jarzębska et al. [13] and Pachla et al. [14] prepared a Zn–1Mg (wt. %) alloy by hydrostatic extrusion. This processing method is performed at ambient temperatures being an advantage of processing zinc alloys as it limits the dynamic recrystallisation processes. Thanks to this effect,

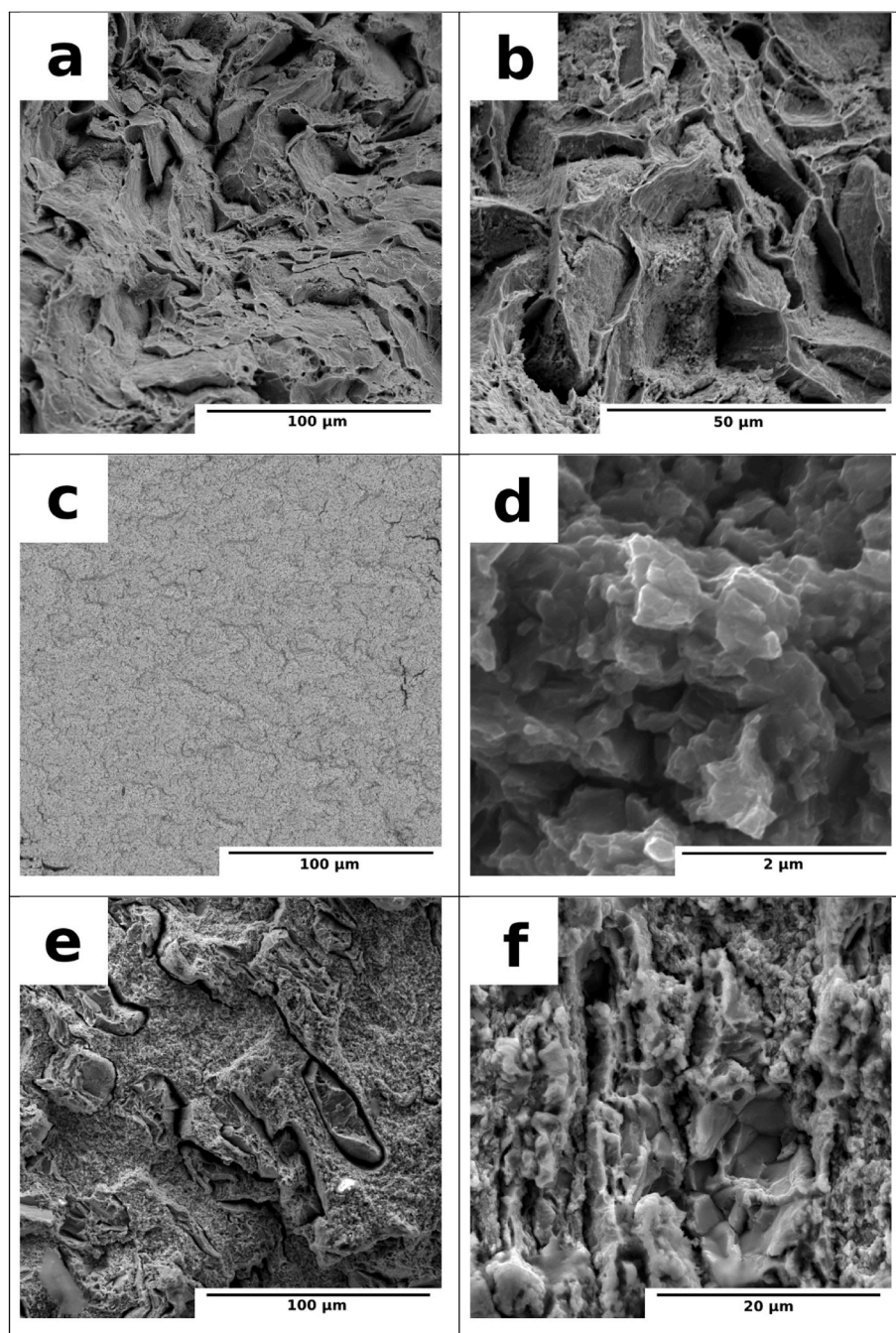


Fig. 14. The fracture surface after the tensile test for the (a,b) $\text{Zn}^{\text{SPS} + \text{Ex}}$, (c,d) $\text{Zn-1Mg}^{\text{SPS} + \text{Ex}}$, (e,f) $\text{Zn} + \text{Zn-1Mg}^{50:50_{\text{SPS} + \text{Ex}}}$ material.

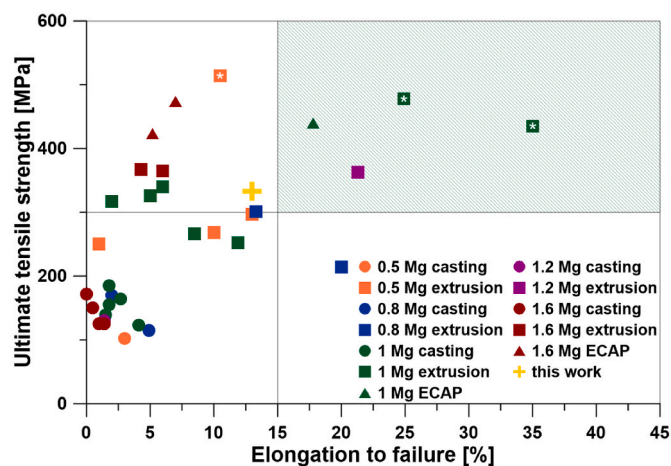
Table 3

The values of the strain hardening exponent and strength coefficient were obtained according to the Hollomon equation.

	K	n
$\text{Zn}^{\text{Ex} + \text{SPS}}$	182 ± 18	0.08 ± 0.01
$\text{Zn-1Mg}^{\text{Ex} + \text{SPS}}$	1052 ± 30	0.27 ± 0.04
$\text{Zn} + \text{Zn-1Mg}^{\text{Ex} + \text{SPS}}$	588 ± 44	0.17 ± 0.05

these works presented materials that reached the UTS of 435 MPa and 478 MPa and the elongation to failure equal to 35 % and 24.9 %, respectively [13,14]. Both of these materials are satisfactory for biodegradable implant applications. In the work of Chen et al. [15], the Zn-1Mg material prepared by equal channel angular pressing (ECAP)

was studied. This method effectively refines the microstructure of the material and, therefore, significantly improved mechanical properties can be achieved. The processing by ECAP resulted in the ultimate tensile strength of 440 MPa and the elongation to failure of 17.8 % [15]. Although not reaching these characteristics, the material presented in this work exhibits an excellent combination of strength and elongation to failure. It is worth mentioning that the real content of Mg in the $\text{Zn} + \text{Zn-1Mg}^{50:50_{\text{SPS} + \text{Ex}}}$ is 0.5 wt %, so half or less compared to the amount presented in the studies of Shen [39], Jarzewska [13], Pachla [14] and Chen [15]. Furthermore, no Zn-0.5 Mg alloy has been able to achieve such a combination of mechanical performance indicating the importance of the designed structure for tailoring appropriate mechanical properties.



*ECAP = Equal Channel Angular Pressing

Fig. 15. Tensile mechanical properties of Zn–Mg materials. Mechanical properties recommended for orthopaedic biodegradable implants are identified by the green part of the graph [5]. Contents of magnesium are given in weight %. The materials marked with * were prepared by hydrostatic extrusion. Data were obtained from several studies [2,6,8–17,39–42].

5. Conclusions

This research endeavours to enhance the mechanical attributes of the Zn–Mg alloy system through the development of materials characterised by a harmonic-like structure, which integrates soft regions within an ultrafine-grained three-dimensional skeleton. Materials were successfully synthesised from initial zinc powder (with a particle size range of 63–100 μm) and Zn–1Mg alloy powder (particle size <45 μm) followed by consolidation through spark plasma sintering and further densification via extrusion.

The observed microstructure of SPS products featured domains of pure zinc encapsulated within a Zn–1Mg matrix, with grain sizes in the order of hundreds of nanometers. Critical observations at the interface between the soft and hard domains revealed the presence of brittle oxide shells, detrimental to the desired mechanical performance.

The hot extrusion process showed itself as a suitable technique to disrupt these oxide shells into small particles. Among others, the extruded Zn + Zn–1Mg material with the 50:50 ratio of zinc and Zn–1Mg domain exhibited the most benefits regarding the homogeneity of microstructure, the content of hard and soft domains and obtained mechanical properties corresponding to the compressive strength of 437 ± 12 MPa and tensile strength of 333 ± 7 MPa. Also, the elongation to fracture of extruded material reached a promising value of 13 ± 2 %. These results are even highlighted by the very low total content of Mg (0.5 wt %) in the material.

Although further research is necessary to optimise harmonic structures in Zn-based materials and shift the mechanical performance to higher levels, the presented work brings an interesting and functional concept of tailoring the mechanical behaviour of biodegradable zinc-based alloys.

Data availability

The data used in this article are located in the Zenodo repository under link <https://doi.org/10.5281/zenodo.12514533>.

Declaration of competing interest

The authors declare that they have no known competing financial interests or personal relationships that could have appeared to influence the work reported in this paper.

Acknowledgement

This research was supported by the Czech Science Foundation (project no. 21–11439K) and by the project "Mechanical Engineering of Biological and Bio-inspired Systems", funded as project No. CZ.02.01.01/00/22_008/0004634 by Programme Johannes Amos Comenius, call Excellent Research. Furthermore, this work was carried out within the framework of the Slovenian Research Agency ARIS project N2-0182 "Development of advanced bioabsorbable Zn-based materials by powder metallurgy techniques." and ARIS program P2 0132 "Physics and Chemistry of Metals".

Appendix A. Supplementary data

Supplementary data to this article can be found online at <https://doi.org/10.1016/j.jmrt.2024.06.223>.

References

- [1] Vařák M, Hasler D. Metallothioneins new functional and structural insights. *Curr Opin Chem Biol* 2000;4(2):177–83.
- [2] Vojtech D, Kubasek J, Serak J, Novak P. Mechanical and corrosion properties of newly developed biodegradable Zn-based alloys for bone fixation. *Acta Biomater* 2011;7(9):3515–22.
- [3] Fairweather-Tait SJ. Zinc in human nutrition. *Nutr Res Rev* 1988;1(1):23–37.
- [4] Venezuela J, Dargusch MS. The influence of alloying and fabrication techniques on the mechanical properties, biodegradability and biocompatibility of zinc: a comprehensive review. *Acta Biomater* 2019;87:1–40.
- [5] Heiden M, Walker E, Stanciu L. Magnesium, iron and zinc alloys, the trifecta of bioresorbable orthopaedic and vascular implantation - a review. *J Biotechnol Biomater* 2015;5(2).
- [6] Katarivas Levy G, Goldman J, Aghion E. The prospects of zinc as a structural material for biodegradable implants—a review paper. *Metals* 2017;7(10).
- [7] Okamoto H. Comment on Mg–Zn (magnesium–zinc). *J Phase Equil* 1994;15(1):129–30.
- [8] Kubásek J, Pospíšilová I, Vojtěch D, Jablonská E, Ruml T. Structural, mechanical and cytotoxicity characterization of as-cast biodegradable Zn–xMg (x = 0.8–8.3%) alloys. *Mater Tehnol* 2014;48(5):623–9.
- [9] Gong H, Wang K, Strich R, Zhou JG. In vitro biodegradation behavior, mechanical properties, and cytotoxicity of biodegradable Zn–Mg alloy. *J Biomed Mater Res B Appl Biomater* 2015;103(8):1632–40.
- [10] Kubásek J, Vojtěch D, Jablonska E, Pospisilova I, Lipov J, Ruml T. Structure, mechanical characteristics and in vitro degradation, cytotoxicity, genotoxicity and mutagenicity of novel biodegradable Zn–Mg alloys. *Mater Sci Eng C* 2016;58:24–35.
- [11] Jin H, Yang L, Cui L, Chen L, Lai Y, Guo H, Liu Y. Study on properties of Zn–xMg (x = 0.5, 0.8, 1) alloys for potential stent material. *J Mater Eng Perform* 2022;32(16):7468–79.
- [12] Wang L-Q, Ren Y-P, Sun S-N, Zhao H, Li S, Qin G-W. Microstructure, mechanical properties and fracture behavior of as-extruded Zn–Mg binary alloys. *Acta Metall Sin* 2017;30(10):931–40.
- [13] Jarzębska A, Bieda M, Kawałko J, Rogal E, Koprowski P, Sztwiertnia K, Pachla W, Kulczyk M. A new approach to plastic deformation of biodegradable zinc alloy with magnesium and its effect on microstructure and mechanical properties. *Mater Lett* 2018;211:58–61.
- [14] Pachla W, Przybysz S, Jarzebska A, Bieda M, Sztwiertnia K, Kulczyk M, Skiba J. Structural and mechanical aspects of hypoeutectic Zn–Mg binary alloys for biodegradable vascular stent applications. *Bioact Mater* 2021;6(1):26–44.
- [15] Chen H, Xiao Y, Lu W, Ji H, Yang Y, Liang B, Cui X. Developing a Zn alloy with high strength and uniform elongation as a biomedical device. *Mater Res Express* 2023;10(10).
- [16] Liu H, Huang H, Zhang Y, Xu Y, Wang C, Sun J, Jiang J, Ma A, Xue F, Bai J. Evolution of Mg–Zn second phases during ECAP at different processing temperatures and its impact on mechanical properties of Zn–1.6Mg (wt.%) alloys. *J Alloys Compd* 2019;811.
- [17] Huang H, Liu H, Wang L-S, Li Y-H, Agbedor S-O, Bai J, Xue F, Jiang J-H. A high-strength and biodegradable Zn–Mg alloy with refined ternary eutectic structure processed by ECAP. *Acta Metall Sin* 2020;33(9):1191–200.
- [18] Necas D, Marek I, Pinc J, Vojtech D, Kubasek J. Advanced zinc-magnesium alloys prepared by mechanical alloying and spark plasma sintering. *Materials* 2022;15(15).
- [19] Zhu Y, Wu X. Heterostructured materials. *Prog Mater Sci* 2023;131.
- [20] Zhu Y, Ameyama K, Anderson PM, Beyerlein IJ, Gao H, Kim HS, Lavernia E, Mathaudhu S, Mughrabi H, Ritchie RO, Tsuji N, Zhang X, Wu X. Heterostructured materials: superior properties from hetero-zone interaction. *Mater Res Lett* 2020;9(1):1–31.
- [21] Wu X, Zhu Y. Heterogeneous materials: a new class of materials with unprecedented mechanical properties. *Mater Res Lett* 2017;5(8):527–32.
- [22] Sharma B, Dirras G, Ameyama K. Harmonic structure design: a strategy for outstanding mechanical properties in structural materials. *Metals* 2020;10(12).

- [23] Ameyama K, Cazes F, Couque H, Dirras G, Kikuchi S, Li J, Momprou F, Mondal K, Orlov D, Sharma B, Tingaud D, Vajpai SK. Harmonic structure, a promising microstructure design. *Mater Res Lett* 2022;10(7):440–71.
- [24] Shimokawa T, Hasegawa T, Kiyota K, Niiyama T, Ameyama K. Heterogeneous evolution of lattice defects leading to high strength and high ductility in harmonic structure materials through atomic and dislocation simulations. *Acta Mater* 2022; 226.
- [25] Pinc J, Školáková A, Veřtát P, Duchoň J, Kubásek J, Lejček P, Vojtěch D, Čapek J. Microstructure evolution and mechanical performance of ternary Zn-0.8Mg-0.2Sr (wt. %) alloy processed by equal-channel angular pressing. *Mater Sci Eng, A* 2021; 824.
- [26] Al-Azzawi A, Baumli P, Mucsi G. Mechanical alloying and milling. The publications of the MultiScience - XXIX. MicroCAD international scientific conference. 2015.
- [27] Suryanarayana C. Mechanical alloying: a novel technique to synthesize advanced materials, vol. 2019. Research (Wash D C); 2019, 4219812.
- [28] Minárik P, Zemková M, Lukáč F, Bohlen J, Knapek M, Král R. Microstructure of the novel biomedical Mg-4Y-3Nd alloy prepared by spark plasma sintering. *J Alloys Compd* 2020;819.
- [29] Brežina M, Minda J, Doležal P, Krystýnová M, Fintová S, Zapletal J, Wasserbauer J, Ptáček P. Characterization of powder metallurgy processed pure magnesium materials for biomedical applications. *Metals* 2017;7(11).
- [30] Necas D, Kubasek J, Pinc J, Marek I, Donik C, Paulin I, Vojtech D. Ultrafine-grained Zn-Mg-Sr alloy synthesized by mechanical alloying and spark plasma sintering. *Materials* 2022;15(23).
- [31] Zhu Y. Introduction to heterostructured materials: a fast emerging field. *Metall Mater Trans* 2021;52(11):4715–26.
- [32] Wu X, Yang M, Yuan F, Wu G, Wei Y, Huang X, Zhu Y. Heterogeneous lamella structure unites ultrafine-grain strength with coarse-grain ductility. *Proc Natl Acad Sci U S A* 2015;112(47):14501–5.
- [33] Zhang Z, Chen DL. Contribution of Orowan strengthening effect in particulate-reinforced metal matrix nanocomposites. *Mater Sci Eng, A* 2008;483–484:148–52.
- [34] Chen C, Fan S, Niu J, Huang H, Jin Z, Kong L, Zhu D, Yuan G. Alloying design strategy for biodegradable zinc alloys based on first-principles study of solid solution strengthening. *Mater Des* 2021;204.
- [35] Jin H, Zhao S, Guillory R, Bowen PK, Yin Z, Griebel A, Schaffer J, Earley EJ, Goldman J, Drelich JW. Novel high-strength, low-alloys Zn-Mg (<0.1wt% Mg) and their arterial biodegradation. *Mater Sci Eng C* 2018;84:67–79.
- [36] Figueiredo RB, Kawasaki M, Langdon TG. Seventy years of Hall-Petch, ninety years of superplasticity and a generalized approach to the effect of grain size on flow stress. *Prog Mater Sci* 2023;137.
- [37] Zhou Y, Luo Q, Jiang B, Li Q, Pan F. Strength-ductility synergy in Mg98.3Y1.3Ni0.4 alloy processed by high temperature homogenization and rolling. *Scripta Mater* 2022;208.
- [38] Cáceres CH, Davidson CJ, Griffiths JR, Newton CL. Effects of solidification rate and ageing on the microstructure and mechanical properties of AZ91 alloy. *Mater Sci Eng, A* 2002;325(1):344–55.
- [39] Shen C, Liu X, Fan B, Lan P, Zhou F, Li X, Wang H, Xiao X, Li L, Zhao S, Guo Z, Pu Z, Zheng Y. Mechanical properties, in vitro degradation behavior, hemocompatibility and cytotoxicity evaluation of Zn-1.2Mg alloy for biodegradable implants. *RSC Adv* 2016;6(89):86410–9.
- [40] Kubásek J, Vojtěch D, Pospíšilová I, Michalcová A, Maixner J. Microstructure and mechanical properties of the micrograined hypoeutectic Zn-Mg alloy. *Int J Miner Metall Mater* 2016;23(10):1167–76.
- [41] Li HF, Xie XH, Zheng YF, Cong Y, Zhou FY, Qiu KJ, Wang X, Chen SH, Huang L, Tian L, Qin L. Development of biodegradable Zn-IX binary alloys with nutrient alloying elements Mg, Ca and Sr. *Sci Rep* 2015;5:10719.
- [42] Mostaed E, Sikora-Jasinska M, Mostaed A, Loffredo S, Demir AG, Previtali B, Mantovani D, Beanland R, Vedani M. Novel Zn-based alloys for biodegradable stent applications: design, development and in vitro degradation. *J Mech Behav Biomed Mater* 2016;60:581–602.